The Astrophysical Journal, 955:117 (14pp), 2023 October 1 https://doi.org/10.3847/1538-4357/acec71

An Updated Reference Frame for the Galactic Inner Parsec

Jeremy Darling[1], Jennie Paine[1], Mark J. Reid[2], Karl M. Menten[3], Shoko Sakai[4], and Andrea Ghez[4]
[1] Center for Astrophysics and Space Astronomy, Department of Astrophysical and Planetary Sciences, University of Colorado, 389 UCB, Boulder, CO 80309-0389, USA; jeremy.darling@colorado.edu
[2] Center for Astrophysics, Harvard & Smithsonian, 60 Garden Street, Cambridge, MA 02138, USA
[3] Max-Planck-Institut für Radioastronomie, Auf dem Hügel 69, D-53121 Bonn, Germany
[4] UCLA Department of Physics and Astronomy, Los Angeles, CA 90095-1547, USA
Received 2023 March 25; revised 2023 July 28; accepted 2023 July 31; published 2023 September 25

Abstract

Infrared observations of stellar orbits about Sgr A* probe the mass distribution in the inner parsec of the Galaxy and provide definitive evidence for the existence of a massive black hole. However, the infrared astrometry is relative and is tied to the radio emission from Sgr A* using stellar SiO masers that coincide with infrared-bright stars. To support and improve this two-step astrometry, we present new astrometric observations of 15 stellar SiO masers within 2 pc of Sgr A*. Combined with legacy observations spanning 25.8 yr, we reanalyze the relative offsets of these masers from Sgr A* and measure positions and proper motions that are significantly improved compared to the previously published reference frame. Maser positions are corrected for epoch-specific differential aberration, precession, nutation, and solar gravitational deflection. Omitting the supergiant IRS 7, the mean position uncertainties are 0.46 mas and 0.84 mas in R.A. and decl., and the mean proper motion uncertainties are 0.07 mas yr^{-1} and 0.12 mas yr^{-1}, respectively. At a distance of 8.2 kpc, these correspond to position uncertainties of 3.7 and 6.9 au and proper motion uncertainties of 2.7 and 4.6 km s^{-1}. The reference frame stability, the uncertainty in the variance-weighted mean proper motion of the maser ensemble, is 8 μas yr^{-1} (0.30 km s^{-1}) in R.A. and 11 μas yr^{-1} (0.44 km s^{-1}) in decl., which represents a 2.3-fold improvement over previous work and a new benchmark for the maser-based reference frame.

Unified Astronomy Thesaurus concepts: Astrophysical masers (103); Circumstellar masers (240); Silicon monoxide masers (1458); Galactic center (565); Astrophysical black holes (98); Supermassive black holes (1663); Astronomical coordinate systems (82); Radio astrometry (1337); Astrometry (80); Proper motions (1295); Stellar kinematics (1608); Stellar motion (1615)

1. Introduction

Infrared observations of stellar orbits in the vicinity of Sgr A* spanning nearly three decades have demonstrated the presence of a massive black hole in the Galactic center (e.g., Ghez et al. 2008; Genzel et al. 2010). These observations can also probe the mass distribution in the inner parsec, including that of the dark matter and other unseen material (Lacroix 2018; Nampalliwar et al. 2021; Heißel et al. 2022; Yuan et al. 2022). The infrared astrometry has historically relied on a radio-based astrometric reference frame that ties IR-bright stars to the location of Sgr A* via simultaneous observation of SiO maser-emitting stars and the Sgr A* 43 GHz radio continuum (e.g., Menten et al. 1997; Reid et al. 2003, 2007; Yelda et al. 2010; Plewa et al. 2015; Sakai et al. 2019). The predicted positions of these jointly detected stars degrade over time, and the maser-based reference frame must therefore be regularly monitored and updated. It has now been 16 yr since the last published maser observations used for the Galactic center reference frame (Reid et al. 2007, but see Sakai et al. 2019).

Here we present an updated radio reference frame for the Galactic center that incorporates new and legacy Karl G. Jansky Very Large Array (VLA)[5] data (Section 2). We employ new astrometric methods (Section 3) to obtain unprecedented position and proper motion measurements and reference frame stability (Section 4). We examine the error budgets, systematic effects, and possible intrinsic scatter in the astrometry (Section 5), examine trends in the 3D stellar velocities (Section 6), and discuss future work (Section 7). The Appendices discuss time-dependent differential astrometric corrections, provide the complete maser time series, examine alternative proper motion fitting methods, and assess the possibility of underestimated astrometric uncertainties.

Calculations that convert angular offsets to projected physical distances or proper motions to transverse velocities assume a distance to Sgr A* of 8.2 kpc, which is consistent with most recent distance measurements (e.g., Do et al. 2019; Reid et al. 2019; Gravity Collaboration et al. 2021; Leung et al. 2023).

2. Data

Table 1 lists the epochs, observing programs, observed SiO transitions, and beam properties of the legacy and new data sources used to derive astrometric solutions for the stellar SiO masers near Sgr A*. There are additional masers in the field of view, such as those detected by Li et al. (2010) and Paine & Darling (2022), as well as additional maser transitions that are

[5] The National Radio Astronomy Observatory is a facility of the National Science Foundation operated under cooperative agreement by Associated Universities, Inc.

Table 1
SiO Maser Data and Observations

Mean Epoch	Program	v[a]	Beam (mas)	References
1996.413	VLBA BM060	1	1.2×0.9	R03
1998.410	VLA AM592	1	70×30	R03
2000.850	VLA AR451	1	80×40	R03
2006.200	VLA AR588	1	86×33	R07
2008.860	VLA AR678	1	82×35	R22
2011.470	VLA 11A-101	1	97×42	R22
2014.249	VLA 14A-168	1,2	66×30	R22
2020.988	VLA 19A-310	1,2	93×36	P22,D22
2022.227	VLA 22A-328	1,2	82×39	D22

References. R03 = Reid et al. (2003); R07 = Reid et al. (2007); R22 = M. J. Reid (2022, private communication); P22 = Paine & Darling (2022); D22 = this work.
[a] Vibration quantum number (all transitions are $J = 1 - 0$).

not included in this study because they do not have legacy astrometry (Reid et al. 2003, 2007).

2.1. Legacy Data

We employ the VLA and VLBA astrometric measurements of 15 SiO masers presented in Reid et al. (2003) and Reid et al. (2007). These span 1996–2006. In addition, we use the measurements obtained from VLA programs in 2008, 2011, and 2014 by Reid (2022, private communication). We did not use the 1995 VLA data presented in Menten et al. (1997) because the uncertainties in the measured coordinates are an order of magnitude larger than subsequent epochs due to larger synthesized beams.

2.2. New Observations and Data Reduction

New VLA observations were conducted in programs 19A-310 (2020 December 27 or 2020.988) and 22A-328 (2022 March 21, 24, and 28; mean epoch 2022.227). Both used the most extended A configuration and set Sgr A* as the phase center because the SiO masers of interest fall within the primary beam. Both used 3C286 for flux calibration, but 19A-310 used J1733−1304 for bandpass and delay calibration, while 22A-328 used J1924−2914. Rather than switch between the science target field and a complex gain calibrator, the 1.0 ± 0.1 Jy Sgr A* compact continuum was used for in-beam gain calibration in both programs. While the 19A-310 program has been analyzed in Paine & Darling (2022), we reprocess and reanalyze it here in a manner that is consistent with the legacy measurements, particularly 2014.249 (see Table 1), and the treatment of 22A-328 observations described below.

VLA 19A-310 observations spanned 2.25 hr (1.16 hr on-source) using a recording time of 2 s and two circular polarizations. The $v = 0$ $J = 1 - 0$, $v = 1$ $J = 1 - 0$, and $v = 2$ $J = 1 - 0$ transitions of SiO and the $v = 1$ $J = 1 - 0$ transition of ^{29}SiO were observed with 62.5 kHz channels, but only the $v = 1$ and $v = 2$ transitions of SiO at 43.1221 GHz and 42.8206 GHz were detected. Bandwidths were 128 MHz each, except for the $v = 2$ spectral window, which spanned 64 MHz. SiO-16 was not detected in either transition in the 2020 epoch, and IRS 7, IRS 9, and IRS 28 were only detected at $>5\sigma$ in the $v = 1$ transition (IRS 9 $v = 2$ was not observed).

VLA 22A-328 observations spanned 5 hr (3.77 hr on-source) in each of three observing sessions. The $v = 1$ $J = 1 - 0$ and $v = 2$ $J = 1 - 0$ transitions of SiO were observed using 3 s integrations, two circular polarizations, and 100 kHz channels spanning 128 MHz. Only IRS 7 lacked a $>5\sigma$ detection in one of the transitions ($v = 2$).

We used CASA (McMullin et al. 2007) for calibration, imaging, and coordinate measurements. Prior to calibration, the data were averaged in frequency from 62.5 and 100 kHz channels to 187.5 kHz (1.3 km s^{-1}) and 200 kHz (1.4 km s^{-1}) channels and in time from 2 s and 3 s records to 6 s records for the 2020 and 2022 observations, respectively. Using Sgr A* for the complex gain calibration provides in-beam calibration of the masers and forces the Sgr A* continuum to be the phase center. The absolute astrometry is therefore lost, but the reference frame and dynamical quantities of interest can be obtained from the relative coordinate offsets of the masers compared to Sgr A*, so relative astrometry is adequate for our science goals. Sgr A* shows an apparent 6.4 mas yr^{-1} proper motion when compared to background quasars due to the solar orbit about the Galactic center (Reid & Brunthaler 2020; Xu et al. 2022), and its position was updated for each observation.

Imaging used the CASA `tclean` algorithm centered on Sgr A* with postage-stamp image cubes of all maser locations as "outlier" fields. The outlier fields are cleaned simultaneously with Sgr A*. We did not subtract the continuum from the spectral line data. Cleaning was performed down to 5 times the per-channel rms noise in the dirty cubes. All three sessions of 22A-328 were incorporated into a single spectral cube for each SiO transition for each maser. Figure 1 shows all spectra for the $v = 1$ transition. The rms noise per channel was ∼2–3 mJy beam^{-1} in 2020 and ∼1 mJy beam^{-1} in 2022.

To be consistent with previous work by Reid et al. (2003, 2007), and contrary to the *uv*-based fitting used by Paine & Darling (2022), we measure maser positions in the image plane. We used the CASA routine `imfit` to fit 2D Gaussians to measure the centroid of the Sgr A* continuum and each maser in every channel in each transition independently. Maser coordinates were obtained from a variance-weighted average of the channel-by-channel centroids with peak fluxes $>5\sigma$, incorporating both transitions. Sgr A* coordinates were calculated from the variance-weighted channel centroids over the entire continuum. Typical maser coordinate uncertainties are 0.2 mas (1.6 au at 8.2 kpc), which is a substantial improvement over most legacy measurements by a factor of roughly 2–4.

We combined the newly measured maser coordinates with those from the legacy observations listed in Table 1 to form time series spanning up to 25.8 yr. After the astrometric corrections described below are applied to the time series, linear fits provide proper motions.

3. Astrometric Methods

Masers (and stars) in the vicinity of Sgr A* may not appear to be exactly where they physically lie. Light propagation and observer-induced effects such as solar gravitational deflection and aberration can cause the entire field of view to shift, which is not a problem for relative coordinate measurements, but these effects are also differential, causing relative astrometric offsets between objects as observed. In general, any phenomenon that deflects or appears to deflect light rays and depends

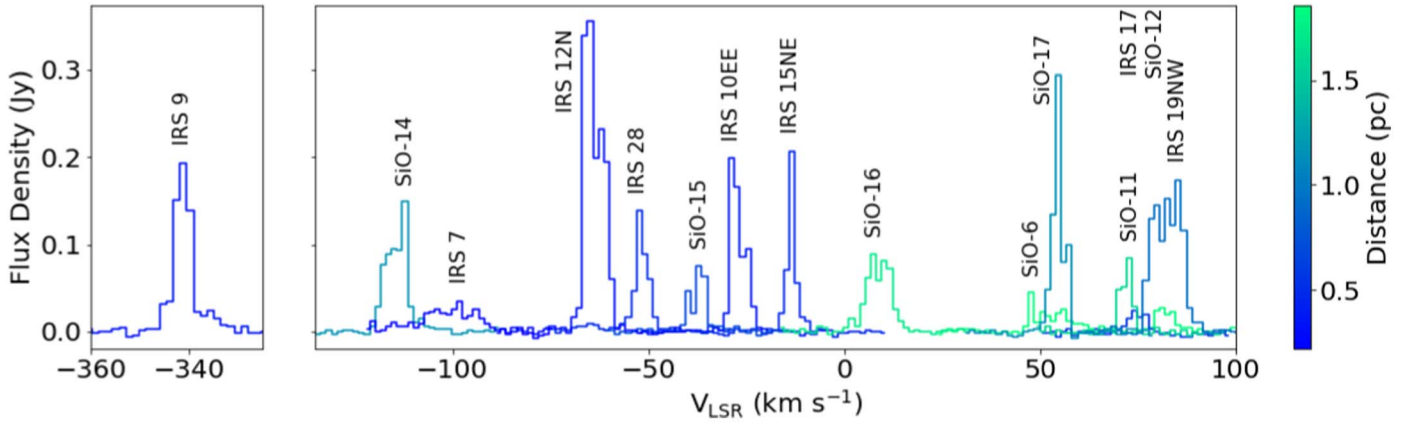

Figure 1. Composite spatially integrated SiO $v = 1$, $J = 1 - 0$ maser spectra from the 2022.227 epoch image cubes. The colors indicate the projected distance from Sgr A*, assuming a Galactic center distance of 8.2 kpc.

on direction will be differential and therefore stretch, shear, or rotate the observed field of view.

It is important to differentiate between relative astrometric offsets from Sgr A* that depend on the observation epoch and those that are stable over time. Epoch-dependent relative offsets must be determined and removed from astrometric time series to obtain proper motions. Time-stable offsets must be quantified in order to determine the actual physical locations of stars for kinematic or dynamical modeling, such as characterizing the metric around the Sgr A* black hole or the mass distribution of the inner parsec (e.g., GRAVITY Collaboration et al. 2022).

Time-dependent differential astrometric offsets include aberration, terrestrial precession-nutation, and solar gravitational deflection. Aberration caused by an observer's motion will be differential because its amplitude depends on direction (e.g., the cosmic microwave background and galaxies show a dipole; Smoot et al. 1977; Ellis & Baldwin 1984; Darling 2022). The dominant contribution is the solar motion within the Galaxy, which produces a steady apparent motion of Sgr A* (Reid & Brunthaler 2020), but the Earth's orbit adds an aberration epicycle that does depend on the observation epoch. Terrestrial precession-nutation involves the secular precession of the celestial pole plus epicycles about this pole, which are necessarily time dependent. Finally, the solar mass causes measurable gravitational deflection, even at large angular offsets, and the solar-Sgr A* angular separation depends on the observation epoch.

Corrections for time-dependent differential offsets were applied to all data, new and legacy, using `astropy.coordinates` tools (Astropy Collaboration et al. 2013; Price-Whelan et al. 2018). Starting with the observed maser offsets and the Sgr A* J2000 coordinates, we calculate the "mean" maser J2000 coordinates. These coordinates include a precession correction from the epoch of observation to J2000 but do not include the above effects from aberration, nutation, or gravitational light deflection. Next, we precess the maser and Sgr A* coordinates from J2000 to the equinox of each observed epoch ("apparent" coordinates) and then transform to a precessed geocentric J2000 coordinate system. The geocentric transformation includes the effects of aberration, the precession and nutation of the Earth's rotation axis, and gravitational deflection of incoming rays (Kaplan 2005). Finally, we subtract the precessed and transformed Sgr A* coordinates from the precessed and transformed maser coordinates to obtain a relative maser offset. To correct for time-dependent differential astrometric offsets, we find the difference between the coordinate offsets obtained from the above transformations and the J2000 coordinate offsets as observed. This difference is then subtracted from the observed coordinate offsets. Figure A1 in Appendix A shows an example of the corrections for one epoch. Time-independent offsets, such as the solar-Galactic center aberration, are not removed by this process. A similar process, using different software, was applied to the SiO maser astrometry used in Sakai et al. (2019) but not to the Reid et al. (2007) results.

These differential corrections generally slightly reduce the scatter in the residual time series after fitting for proper motions. This is encouraging, and suggests that the process is providing reasonable time-dependent astrometry. However, the corrections are typically smaller than the variation in the astrometry, and the proper motions and reference frame stability are not significantly altered compared to the no-corrections case. The magnitude of the differential corrections scales linearly with angular separation from Sgr A* in a given epoch and varies from epoch to epoch. The corrections range from ∼0.1 mas to 4.3 mas in absolute value and are similar to the astrometric uncertainty in each coordinate in each epoch, except for masers with large offsets from Sgr A*. The latter have corrections larger than centroid uncertainties due to the linear scaling of the corrections. Table A1 in Appendix A lists the full astrometric time series and the differential corrections for all masers in all epochs.

IRS 7 requires special treatment: it has supergiant luminosity, its SiO maser emission distribution may span 10 mas, and its $v = 1$ $J = 1 - 0$ maser shows substantial variability, both in flux density and in velocity (Reid et al. 2003, 2007). To wit, the $J = 1 - 0$ maser decreased in brightness by a factor of 8, and the -124 km s^{-1} maser component faded below the flux density of the -103 km s^{-1} component from 1995.49 to 2000.85. The dominant component at -103 km s^{-1} persists through the current epoch (Figure 1), but the $J = 2 - 1$ transition resembles the pre-2000 $J = 1 - 0$ spectrum: it is about 10 times brighter and peaks at roughly -123 km s^{-1} (Paine & Darling 2022). The ALMA $J = 2 - 1$ astrometry in 2015.27 and 2017.72, however, is statistically consistent with temporally bracketing VLA $J = 1 - 0$ astrometry in 2014.18 and 2020.99, which is at odds with the possibility of a shift of the $v = 1$ $J = 1 - 0$ maser emission from one side of the supergiant to the other. We conclude that for the purposes of a

Table 2
SiO Maser Angular Offsets and Proper Motions

Name	$v_{\rm LSR}$ (km s^{-1})	R.A. Offset[a] (arcsec)	Decl. Offset (arcsec)	PM R.A. (mas yr^{-1})	PM Decl. (mas yr^{-1})	χ^2_ν	Reference Epoch	$N_{\rm Obs}$
IRS 9	−341	+5.71043 ± 0.00009	−6.30688 ± 0.00023	+3.080 ± 0.016	+2.291 ± 0.033	1.0	2017.946	8
IRS 7	−114	+0.03330 ± 0.00500	+5.49028 ± 0.00500	−0.002 ± 0.044	−4.665 ± 0.093	1.2	2013.582	6
SiO-14	−111	−7.62578 ± 0.00032	−28.46850 ± 0.00046	+2.073 ± 0.041	−0.969 ± 0.064	4.3	2017.153	8
IRS 12N	−65	−3.27773 ± 0.00013	−6.94708 ± 0.00015	−1.122 ± 0.021	−2.834 ± 0.024	2.8	2019.686	9
IRS 28	−54	+10.49199 ± 0.00030	−5.86884 ± 0.00050	+1.548 ± 0.050	−5.493 ± 0.088	2.9	2014.235	8
SiO-15	−35	−12.46900 ± 0.00029	−11.06769 ± 0.00038	−2.562 ± 0.058	+0.738 ± 0.068	1.1	2017.505	6
IRS 10EE	−28	+7.68504 ± 0.00011	+4.17765 ± 0.00017	+0.070 ± 0.017	−1.984 ± 0.020	2.3	2017.308	9
IRS 15NE	−11	+1.20422 ± 0.00019	+11.25164 ± 0.00028	−1.925 ± 0.019	−5.802 ± 0.028	1.6	2010.230	9
SiO-16	+7	−26.42046 ± 0.00067	−34.47238 ± 0.00124	−0.002 ± 0.093	−1.989 ± 0.170	16.9	2017.089	7
SiO-6	+52	+35.25587 ± 0.00106	+30.68278 ± 0.00227	+2.719 ± 0.113	+2.507 ± 0.248	11.4	2009.959	8
SiO-17	+53	+8.08338 ± 0.00035	−27.66156 ± 0.00065	+2.468 ± 0.052	+2.492 ± 0.108	7.8	2014.935	7
SiO-11	+71	+1.76111 ± 0.00078	+40.30709 ± 0.00151	+1.704 ± 0.131	+1.904 ± 0.230	46.5	2014.160	8
IRS 17	+74	+13.14134 ± 0.00090	+5.55666 ± 0.00148	−1.073 ± 0.165	−1.059 ± 0.240	1.8	2009.404	6
SiO-12	+82	−18.80861 ± 0.00086	+42.48144 ± 0.00177	+1.086 ± 0.177	+1.458 ± 0.310	6.9	2015.756	7
IRS 19NW	+84	+14.57819 ± 0.00033	−18.47510 ± 0.00068	+1.414 ± 0.074	−0.702 ± 0.124	15.0	2019.938	8

Note. Coordinate offsets are with respect to the Sgr A* radio centroid at the reference epoch, which is the position variance-weighted date of the time series (see Section 3). The LSR velocity is approximate; the masers show variability in their spectral peaks and velocity centroids (Reid et al. 2003, 2007; Paine & Darling 2022). The χ^2_ν statistic characterizes the joint weighted LS proper motion fit in both coordinates. The coordinate offset uncertainties in IRS 7 have been manually adjusted to ±5 mas (see Section 3).
[a] This offset is corrected for decl.: it is ΔR.A.cos(decl.).

current and near-future reference frame determination, the proper motion and position of IRS 7 should rely on the last 20 yr of observations and omit those made before the dramatic change in the $J = 1 - 0$ emission. The coordinates and proper motions presented in Table 2 and Figure 3 rely on epochs 2006.200–2022.227, and the coordinate uncertainties in the astrometric solution have been set to ±5 mas to allow for the likely maser offsets from the stellar photocenter, following Reid et al. (2007) and Paine & Darling (2022). Table A1 includes the omitted epochs for posterity.

Proper motion measurements in each coordinate require a linear fit to the now-corrected offset coordinate time series. The offset position ($\Delta\alpha\cos\delta$, $\Delta\delta$) of a given stellar maser with respect to Sgr A* observed in epoch $t_{\rm obs}$ is

$$\Delta\alpha\cos\delta = \Delta\alpha_{\rm ref}\cos\delta_{\rm ref} + \mu_\alpha(t_{\rm obs} - t_{\rm ref}), \quad (1)$$

$$\Delta\delta = \Delta\delta_{\rm ref} + \mu_\delta(t_{\rm obs} - t_{\rm ref}) \quad (2)$$

for offsets $\Delta\alpha_{\rm ref}$ and $\Delta\delta_{\rm ref}$ at reference epoch $t_{\rm ref}$ given proper motions $\mu_{\alpha,\delta}$. We do not include curvature in the fits, which would correspond to acceleration (see Paine & Darling 2022 for that analysis and limits on accelerations). After exploring several fitting methods, described in Appendix B, we chose the simplest: linear variance-weighted least-squares (LS) fits using a reference epoch as the intercept of the linear fit. The reference epoch $t_{\rm ref}$ is the variance-weighted mean date in the time series, where the error variance is the sum in quadrature of the coordinate uncertainties of each epoch. The "intercept" of each proper motion fit to the coordinate time series refers to the coordinates of the maser at the reference epoch. This method generally shows negligible correlation between the slope and intercept of the linear fit. The proper motion parameters also show negligible correlation between R.A. and decl., which are fit jointly. See Appendix B for details.

4. Results

Table 2 lists the local standard of rest (LSR) velocity of each maser (see Paine & Darling 2022 for a detailed study), coordinate offsets from Sgr A* at the reference epoch for each maser, the proper motions in each coordinate, a reduced χ^2 statistic for the joint proper motion fit, the reference epoch, and the number of epochs used for the fits. Figure 2 shows an overview of the maser locations and proper motions and indicates whether masers are redshifted or blueshifted along the line of sight. Figure 3 shows the coordinate time series, proper motions, and linear fit residuals for each maser. To obtain the coordinate offsets from Sgr A* for a given stellar maser at a specific time, one would employ the parameters presented in Table 2 in Equations (1) and (2).

Most masers have 7–9 epochs in their time series (SiO-15 and IRS 17 have six, and for IRS 7 we use six), and the post-2000 epochs tend to include more masers. The per-epoch uncertainty in coordinates ranges from 0.1 mas to 8.1 mas, with uncertainties uniformly smaller for R.A. than for decl. due to a north–south elongated synthesized beam. Uncertainties tend to be larger in earlier epochs (less sensitivity and shorter integration times) and for fainter masers (lower signal-to-noise). Table A1 lists the coordinates for each maser in every epoch. The mean uncertainty in the offset coordinate of the masers in the reference epoch is 0.46 mas in R.A. and 0.84 mas in decl., excluding IRS 7 (see Section 3). These correspond to 3.7 au and 6.9 au, respectively, at 8.2 kpc.

The formal uncertainties in the measured position of Sgr A* are 1 μas and 2 μas in R.A. and decl. in epoch 2022.227 and are therefore negligible compared to the uncertainties in the maser coordinates. It is important to note that these very small uncertainties in the Sgr A* position are strictly statistical, and the coordinates of Sgr A* are assigned a priori because it is the phase center used for complex gain calibration.

However, recent work by Xu et al. (2022) found a ∼30 mas offset from the canonical absolute position of Sgr A* (Reid & Brunthaler 2020). This causes second-order astrometric offsets

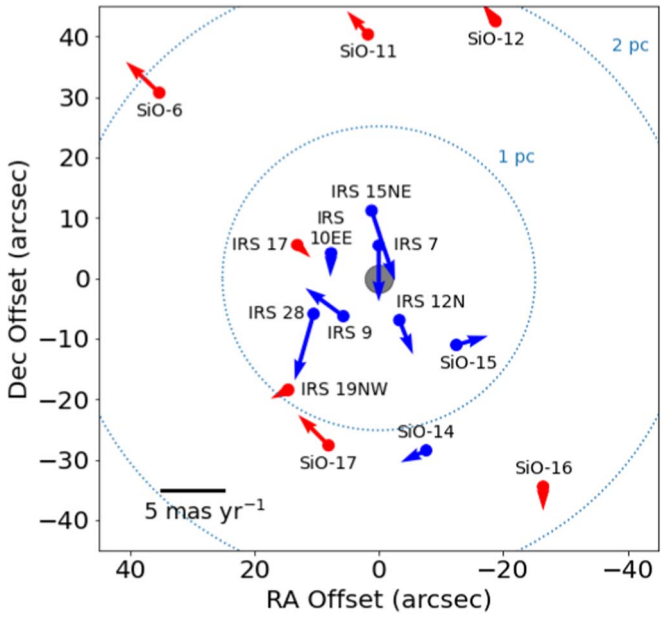

Figure 2. Locations in epoch 2022.227 and proper motions of the stellar SiO masers used for the Galactic center astrometric reference frame (Table 2 and Figure 3). The color indicates the sign of the stellar radial velocities (red is positive; blue is negative). The gray circle marks Sgr A* (not to scale). Projected distances assume a Galactic center distance of 8.2 kpc, and the R.A. offset is corrected for decl.

in the maser positions of order 30 mas $\times \Delta\theta$ where $\Delta\theta$, expressed in radians, is the angular offset from Sgr A*. For the masers presented here, the error is roughly 1–7 μas. This is negligible compared to other uncertainties and systematics, and therefore no correction was applied to the astrometry.

The mean maser proper motion uncertainties are 0.07 mas yr^{-1} in R.A. and 0.12 mas yr^{-1} in decl., corresponding to 2.7 and 4.6 km s^{-1}. As seen in Figure 3, the residuals from the linear time series fits often have significant outliers. These outliers are not consistent across all masers at a fixed epoch (i.e., there do not seem to be epochs with bad astrometry), and they are not restricted to particular stars or coordinate directions. Residuals are often within roughly 1–2 mas (Figure 3); 1 mas corresponds to ∼8 au, which is the typical size of SiO maser distributions around evolved stars (Cotton et al. 2008). Residuals can, however, be as large as ∼5 mas or ∼40 au (Figure 3). The nature of the variation in residuals remains unknown but suggests a systematic effect that should be addressed in future work. It is clear, however, from these long time baselines that astrometric trends (i.e., proper motions) can be measured despite substantial single-epoch departures.

Among the best-measured masers are the bright ones: IRS 9, IRS 12N, and IRS 10EE, which reach coordinate uncertainties of 0.09–0.13 mas (0.7–1.1 au) in R.A. and 0.15–0.23 mas (1.2–1.9 au) in decl. These uncertainties are smaller than the expected size of the maser-emitting regions in the stellar atmospheres. The proper motions of these masers have uncertainties of 0.016–0.021 mas yr^{-1} (0.6–0.8 km s^{-1}) in R.A. and 0.021–0.033 mas yr^{-1} (0.8–1.3 km s^{-1}) in decl., showing that it is possible to reach sub-kilometer per second precision in measurements of transverse velocity (also demonstrated by Paine & Darling 2022).

The reference frame stability, the uncertainty in the variance-weighted mean proper motion of the maser ensemble, is 8 μas yr^{-1} in R.A. and 11 μas yr^{-1} in decl. or 0.30 km s^{-1} in R.A., and 0.44 km s^{-1} in decl. This sub-kilometer per second measurement is 2.3 times smaller than the previous value (Sakai et al. 2019) and represents a new benchmark for the maser-based reference frame. This new reference frame stability is in agreement with the predictions made by Yelda et al. (2010) and Sakai et al. (2019) and should enable observation of the apocenter shift of the star S0-2 caused by relativistic prograde precession (Schwarzschild precession; Weinberg et al. 2005). It should be noted that this general relativistic effect was detected for S0-2 (aka S2) by the GRAVITY Collaboration et al. (2020), but the precision-limiting factor in the measurement was the radio-to-infrared reference frame conversion of Plewa et al. (2015).

5. Discussion

The astrometry in this and previous work relies on fitting Gaussian brightness distributions to planes in maser image-velocity cubes. In contrast, Paine & Darling (2022) uses *uv*-based fitting, often of several masers simultaneously. The per-epoch astrometry is generally in agreement between the two methods, including for the 2020.988 epoch that is included in both studies. The derived proper motions also show good agreement although the Paine & Darling (2022) time baseline is shorter. However, this study utilized additional epochs, some of which provided 86 GHz maser-based positions.

For many masers—but not all—the scatter about the linear proper motion fit is larger than the formal uncertainties would suggest; i.e., $\chi^2_\nu \gg 1$ (Table 2). That this is not consistently true for all masers suggests that there is no consistent systematic effect influencing the astrometry, and there do not appear to be specific outlier epochs. Possible explanations for the offsets include physical and instrumental effects, but it is difficult to identify systematics that could produce the observed magnitude of the offsets that are not consistent across all masers or limited to specific epochs. Stellar winds, pulsation, maser variability, and stellar companions are possible sources of real offsets in SiO masing regions, but these are unlikely to produce the few milliarcsecond single-epoch departures from the observed proper motion trends. One milliarcsecond is equivalent to 8.2 au, roughly the diameter of the stellar maser-emitting regions. Instrumental or calibration systematics should generally affect all masers in a given epoch and might scale with distance from Sgr A*. It is noteworthy that the masers with the highest χ^2_ν values are all redshifted and generally at the largest separations from Sgr A*.

Regardless of the source of the astrometric variation, one could examine the magnitude and impact of an intrinsic scatter added in quadrature to the measurement uncertainties. In Appendix C, we examine expanded uncertainties (EUs) in the time series and find that while larger uncertainties are favored to fit a linear secular trend model in maser offsets from Sgr A* for 60% of the maser coordinates, the resultant proper motions are formally consistent with those obtained from the weighted LS fits using the original measurement uncertainties.

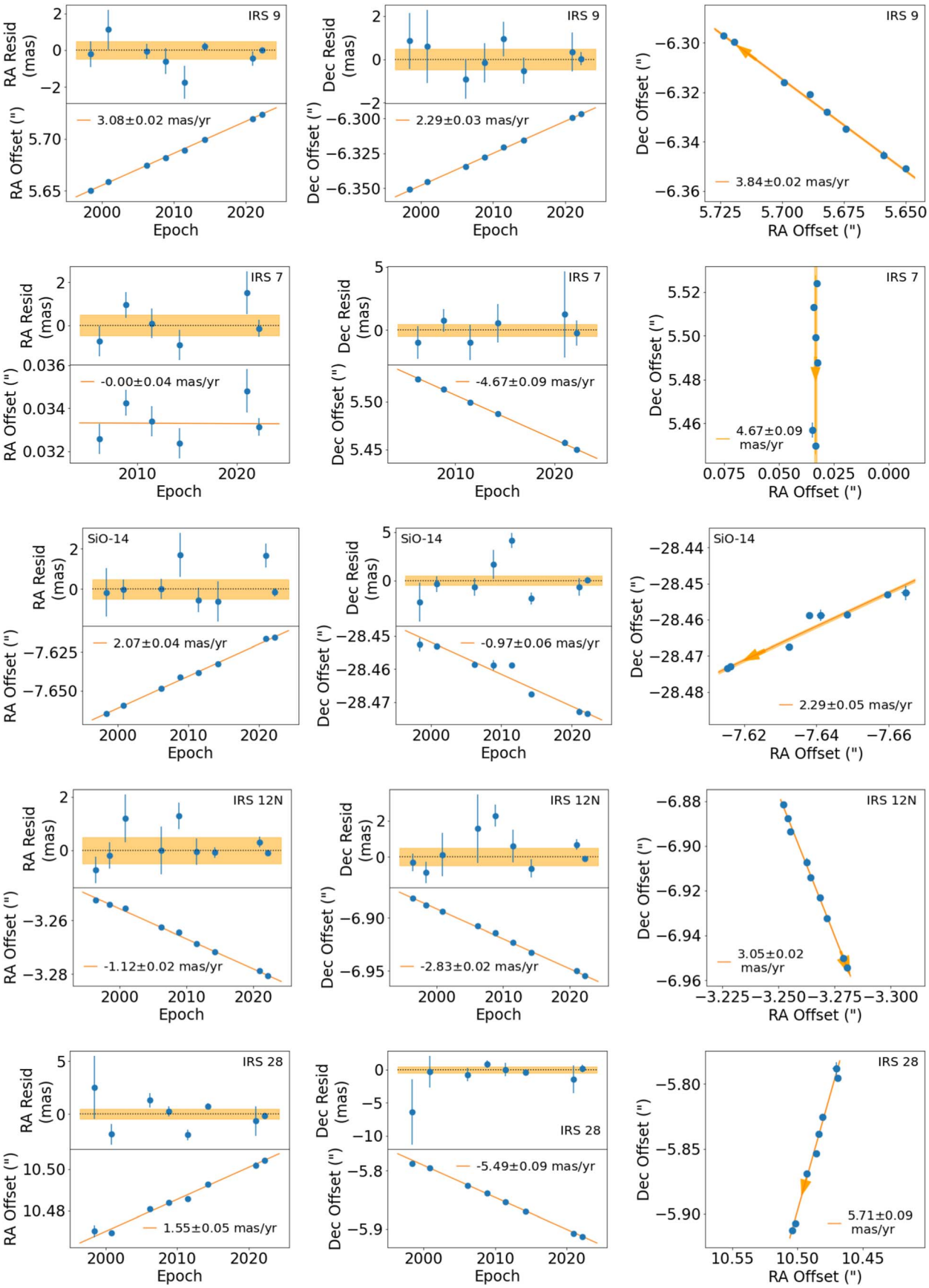

Figure 3. Left and center columns: time series in each coordinate for each stellar maser. The lower panel for each shows the coordinate offset from Sgr A* and the weighted LS linear proper motion fit. The upper panel shows the best-fit residual vs. epoch. The shaded region indicates ±4 au. R.A. offsets are true angular offsets (i.e., they are corrected for cos(decl.)). Right column: sky tracks for the masers. The arrows indicate the direction of the 2D proper motion.

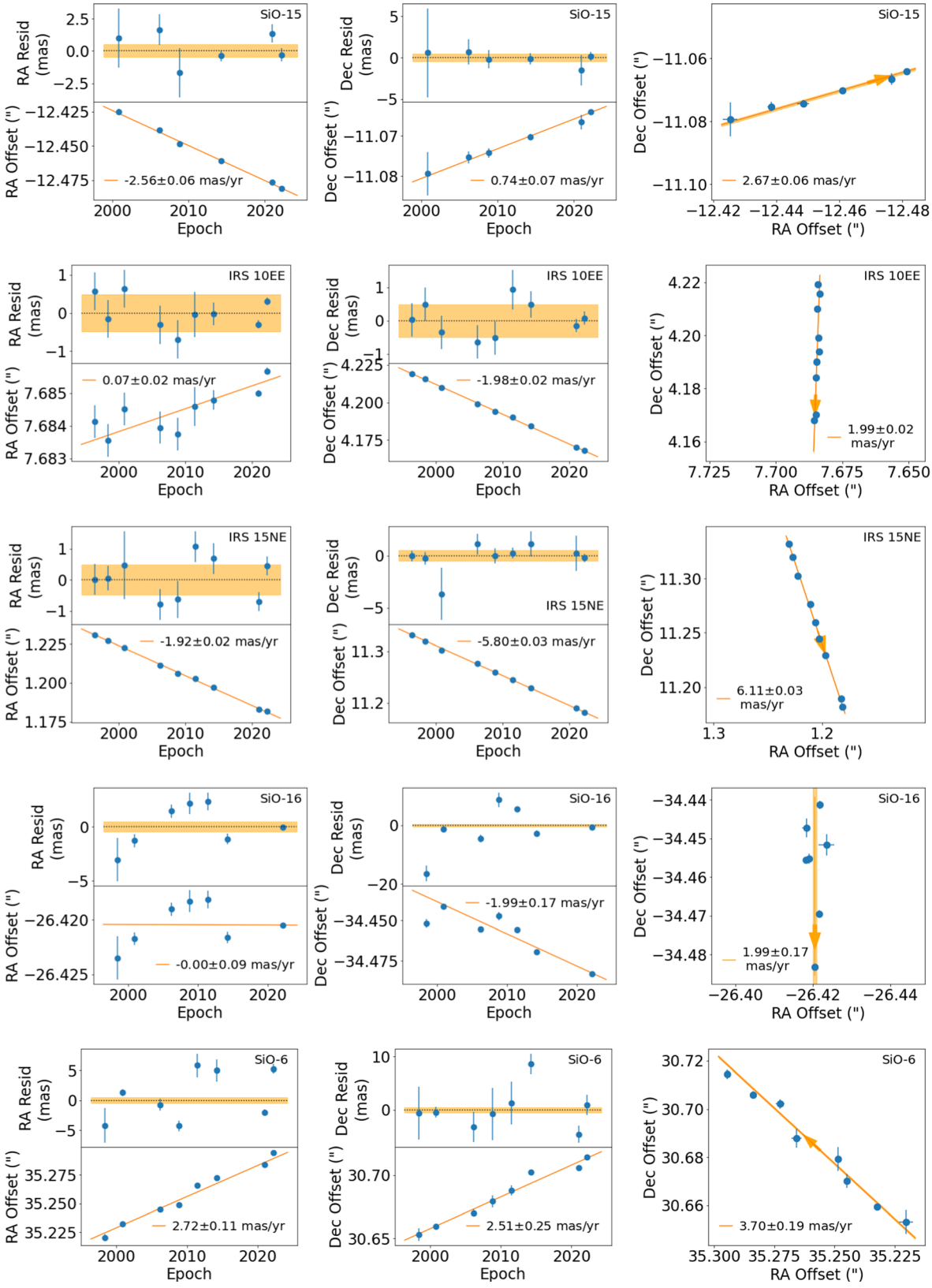

Figure 3. (Continued.)

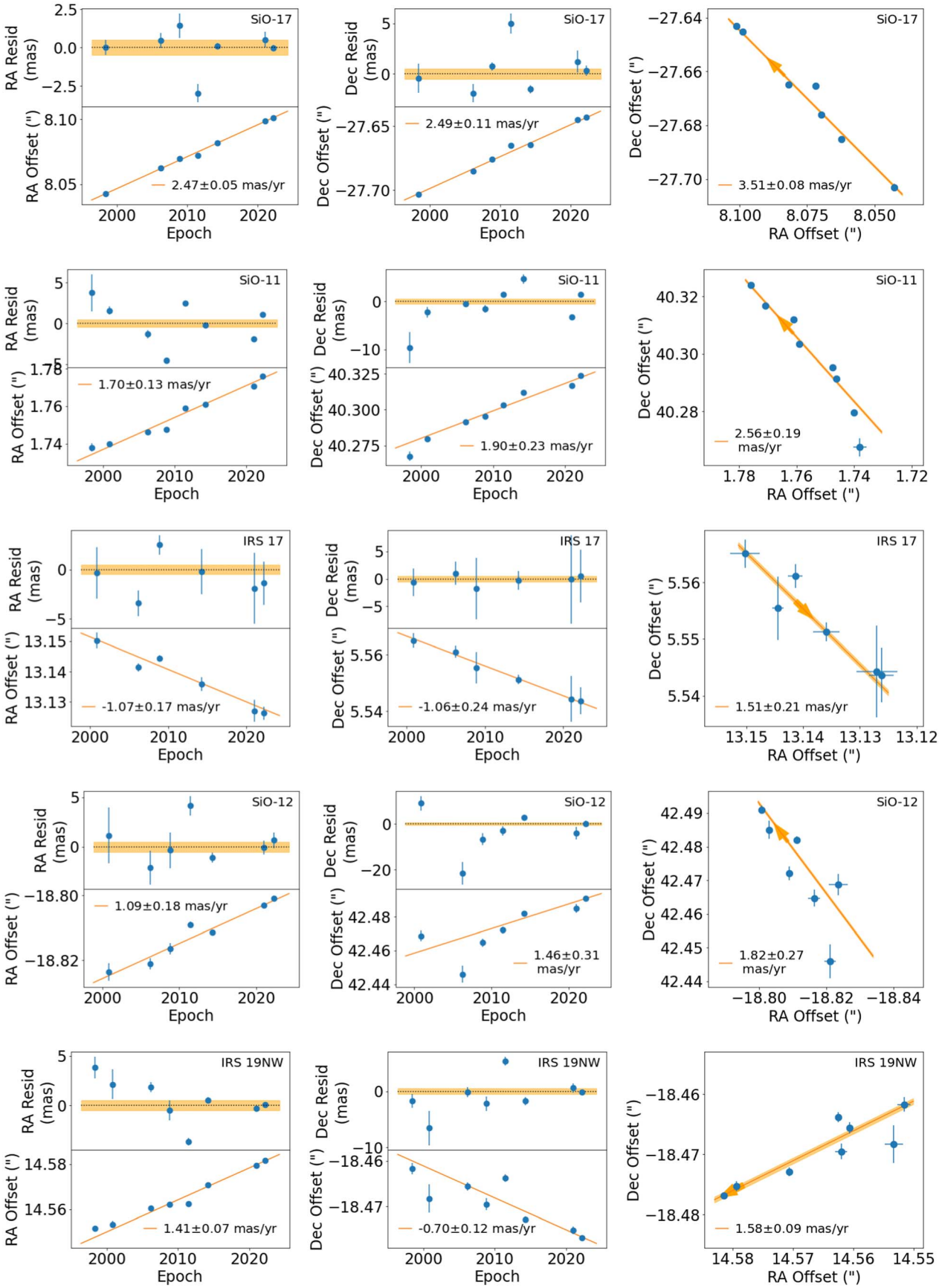

Figure 3. (Continued.)

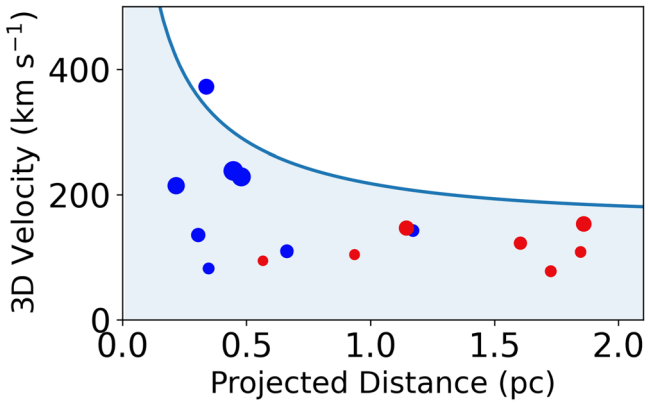

Figure 4. Three-dimensional velocity of stellar masers vs. projected distance from Sgr A*. Point color indicates the sign of the radial velocities (red is redshifted; blue is blueshifted). The size of the points scales linearly with the transverse velocity, spanning 59–241 km s^{-1}. Velocity error bars are uniformly smaller than the data points. The blue line indicates the upper bound on 3D velocity based on the enclosed stellar and black hole masses (see Section 6 and Equation (3)). Projected distances assume a Galactic center distance of 8.2 kpc.

6. Analysis

Given the mass interior to the projected distance from Sgr A*, $M_{\rm encl}$, the 3D velocity of a bound orbit has an upper limit

$$v \leqslant \left(\frac{2GM_{\rm encl}}{r_{\rm proj}}\right)^{1/2}. \quad (3)$$

The enclosed mass is the sum of the black hole mass, combined stellar mass, and any other constituents such as gas and dark matter. In Figure 4 we compare the measured 3D velocities to this upper bound assuming $M_{\rm BH} = 4.3 \times 10^6\ M_\odot$ (GRAVITY Collaboration et al. 2022) and the maximal stellar mass at 1 pc described by Schödel et al. (2018). All stars except IRS 9, which may be unbound (Reid et al. 2007), lie below this locus, in agreement with the mass limits obtained by Paine & Darling (2022). It is interesting that the blueshifted masers tend to be closer in projection to Sgr A* than the redshifted masers although the transverse velocity vectors do not show preferential radial or azimuthal trends (Figure 2). Three-dimensional velocities trend larger with smaller projected radius, as one would expect.

7. Conclusions

Using new and legacy VLA observations, we have updated the SiO stellar maser astrometric reference frame relative to the Sgr A* 43 GHz radio continuum. Much of the astrometry represents new benchmarks in precision, including sub-kilometer per second measurements of transverse velocity for some masers and $\sim$10 μas yr^{-1} reference frame stability. There are, however, significant single-epoch coordinate outliers from proper motion trends for many masers that remain unexplained but provide opportunities to further improve the astrometry if the systematic effects can be quantified and corrected. We have also demonstrated the value of continued and higher-cadence maser monitoring.

Acknowledgments

J.D. and J.P. acknowledge support from NSF grant AST-1908122. S.S. and A.G. acknowledge support from the Gordon & Betty Moore Foundation and NSF grant AST-1909554. We thank the anonymous referee for helpful feedback. This research made use of NumPy (van der Walt et al. 2011), Matplotlib (Hunter 2007), and Astropy,[6] a community-developed core Python package for Astronomy (Astropy Collaboration et al. 2013; Price-Whelan et al. 2018).

Facilities: VLA, VLBA.

Software: CASA (McMullin et al. 2007), astropy (Astropy Collaboration et al. 2013; Price-Whelan et al. 2018), NumPy (van der Walt et al. 2011), Matplotlib (Hunter 2007), `lmfit` (Newville et al. 2021), `emcee` (Foreman-Mackey et al. 2013), CARTA (Comrie et al. 2021).

Appendix A
Differential Astrometric Offsets

As discussed in Section 3, we correct each astrometric epoch for differential aberration, terrestrial precession-nutation, and solar gravitational deflection. The net effect of these time-dependent differential astrometric corrections are offset vectors (ΔR.A. cos(decl.), Δdecl.) with amplitudes that depend linearly on the angular distance from Sgr A* and represent a superposition of radial offsets and rotation. For example, Figure A1 shows the offset vectors for the 1998.410 epoch. The vector amplitudes are not constant in time but always scale as a group for each epoch. Table A1 lists the corrections that have been applied to the offsets from Sgr A* for each maser in each epoch.

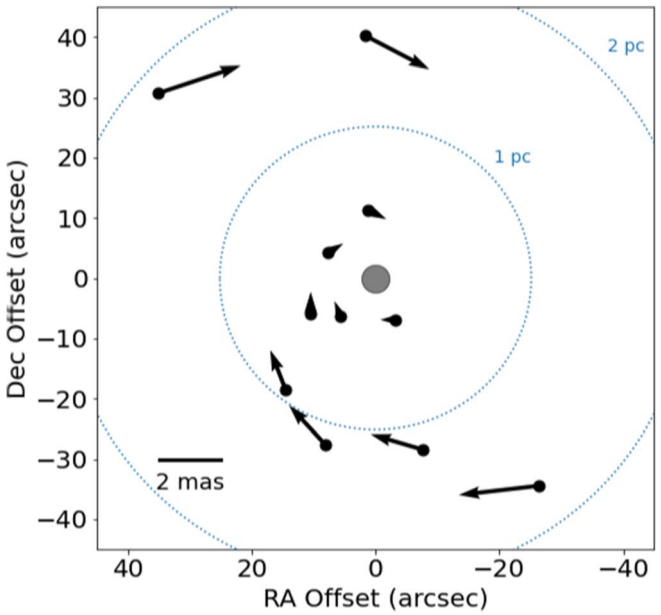

Figure A1. Example differential coordinate offsets of the stellar SiO masers used for the Galactic center astrometric reference frame. This is epoch 1998.410. The vector field includes rotation and a radial component. The amplitude scales linearly with angular distance from Sgr A*. The gray circle marks Sgr A* (not to scale). Projected distances assume a Galactic center distance of 8.2 kpc, and the R.A. offset is corrected for decl.

[6] http://www.astropy.org

Table A1
SiO Maser Coordinate Time Series and Differential Corrections

Name	Epoch	R.A. Offset[a] (arcsec)	Decl. Offset (arcsec)	ΔR.A.[a] (mas)	ΔDecl. (mas)
IRS 9	1998.410	5.6500 ± 0.0007	−6.3508 ± 0.0013	0.2	0.5
	2000.850	5.6589 ± 0.0011	−6.3454 ± 0.0017	0.1	−0.7
	2006.200	5.6742 ± 0.0004	−6.3347 ± 0.0009	−0.6	0.6
	2008.860	5.6818 ± 0.0007	−6.3279 ± 0.0009	0.1	−0.6
	2011.470	5.6887 ± 0.0009	−6.3208 ± 0.0008	0.4	0.3
	2014.249	5.6993 ± 0.0002	−6.3159 ± 0.0006	−0.5	0.7
	2020.988	5.7193 ± 0.0004	−6.2996 ± 0.0009	−0.4	−0.2
	2022.227	5.7236 ± 0.0001	−6.2971 ± 0.0003	−0.5	0.7
IRS 7[b]	1998.410	0.0378 ± 0.0043	5.5495 ± 0.0014	−0.3	−0.2
	2000.850	0.0342 ± 0.0016	5.5414 ± 0.0030	0.2	0.4
	2006.200	0.0326 ± 0.0007	5.5237 ± 0.0013	0.0	−0.5
	2008.860	0.0343 ± 0.0006	5.5131 ± 0.0009	0.2	0.3
	2011.470	0.0334 ± 0.0007	5.4992 ± 0.0014	−0.3	0.0
	2014.249	0.0324 ± 0.0007	5.4877 ± 0.0015	−0.1	−0.5
	2020.988	0.0348 ± 0.0010	5.4570 ± 0.0034	0.3	−0.1
	2022.227	0.0331 ± 0.0004	5.4497 ± 0.0010	−0.0	−0.5
SiO-14	1998.410	−7.6648 ± 0.0012	−28.4526 ± 0.0020	1.7	0.5
	2000.850	−7.6596 ± 0.0005	−28.4531 ± 0.0008	−1.7	−1.5
	2006.200	−7.6485 ± 0.0005	−28.4585 ± 0.0009	0.7	2.8
	2008.860	−7.6413 ± 0.0011	−28.4588 ± 0.0015	−1.7	−1.4
	2011.470	−7.6381 ± 0.0006	−28.4588 ± 0.0008	1.5	−0.6
	2014.249	−7.6324 ± 0.0010	−28.4675 ± 0.0006	1.1	2.6
	2020.988	−7.6162 ± 0.0006	−28.4729 ± 0.0009	−1.4	0.9
	2022.227	−7.6154 ± 0.0002	−28.4734 ± 0.0003	0.9	2.8
IRS 12N	1996.413	−3.2523 ± 0.0005	−6.8814 ± 0.0005	0.4	0.0
	1998.410	−3.2541 ± 0.0005	−6.8876 ± 0.0006	0.5	0.0
	2000.850	−3.2554 ± 0.0009	−6.8936 ± 0.0012	−0.5	−0.3
	2006.200	−3.2626 ± 0.0009	−6.9073 ± 0.0019	0.3	0.7
	2008.860	−3.2643 ± 0.0005	−6.9141 ± 0.0006	−0.5	−0.3
	2011.470	−3.2686 ± 0.0005	−6.9232 ± 0.0009	0.4	−0.2
	2014.249	−3.2717 ± 0.0002	−6.9323 ± 0.0005	0.4	0.6
	2020.988	−3.2789 ± 0.0002	−6.9501 ± 0.0003	−0.3	0.3
	2022.227	−3.2807 ± 0.0001	−6.9544 ± 0.0001	0.4	0.7
IRS 28	1998.410	10.4700 ± 0.0030	−5.7883 ± 0.0050	−0.0	0.7
	2000.850	10.4694 ± 0.0010	−5.7956 ± 0.0024	0.4	−0.8
	2006.200	10.4809 ± 0.0007	−5.8254 ± 0.0010	−1.1	0.5
	2008.860	10.4839 ± 0.0005	−5.8385 ± 0.0006	0.4	−0.8
	2011.470	10.4857 ± 0.0005	−5.8536 ± 0.0010	0.4	0.5
	2014.249	10.4927 ± 0.0003	−5.8693 ± 0.0005	−0.9	0.7
	2020.988	10.5018 ± 0.0014	−5.9074 ± 0.0021	−0.5	−0.5
	2022.227	10.5042 ± 0.0003	−5.9125 ± 0.0006	−1.0	0.6
SiO-15	2000.850	−12.4253 ± 0.0023	−11.0794 ± 0.0054	−1.3	−0.2
	2006.200	−12.4384 ± 0.0012	−11.0753 ± 0.0015	1.2	1.1
	2008.860	−12.4486 ± 0.0019	−11.0743 ± 0.0011	−1.2	−0.1
	2014.240	−12.4610 ± 0.0004	−11.0702 ± 0.0007	1.3	0.9
	2020.980	−12.4765 ± 0.0007	−11.0666 ± 0.0018	−0.5	0.8
	2022.220	−12.4814 ± 0.0005	−11.0641 ± 0.0005	1.3	1.1
IRS 10EE	1996.413	7.6841 ± 0.0005	4.2191 ± 0.0005	−0.4	0.3
	1998.410	7.6836 ± 0.0005	4.2156 ± 0.0005	−0.5	0.3
	2000.850	7.6845 ± 0.0005	4.2099 ± 0.0005	0.7	−0.0
	2006.200	7.6839 ± 0.0005	4.1990 ± 0.0005	−0.7	−0.4
	2008.860	7.6837 ± 0.0005	4.1939 ± 0.0005	0.7	−0.1
	2011.470	7.6846 ± 0.0006	4.1902 ± 0.0006	−0.2	0.4
	2014.249	7.6848 ± 0.0003	4.1842 ± 0.0004	−0.8	−0.3
	2020.988	7.6850 ± 0.0001	4.1702 ± 0.0002	0.1	−0.5
	2022.227	7.6857 ± 0.0001	4.1680 ± 0.0002	−0.8	−0.4
IRS 15NE	1996.413	1.2308 ± 0.0005	11.3318 ± 0.0005	−0.6	−0.3
	1998.410	1.2270 ± 0.0004	11.3200 ± 0.0006	−0.6	−0.3
	2000.850	1.2227 ± 0.0011	11.3024 ± 0.0025	0.6	0.7
	2006.200	1.2112 ± 0.0005	11.2761 ± 0.0010	−0.1	−1.1
	2008.860	1.2062 ± 0.0006	11.2596 ± 0.0007	0.6	0.6
	2011.470	1.2029 ± 0.0005	11.2447 ± 0.0005	−0.6	0.1
	2014.249	1.1972 ± 0.0005	11.2295 ± 0.0012	−0.3	−1.1
	2020.988	1.1828 ± 0.0003	11.1894 ± 0.0017	0.6	−0.2
	2022.227	1.1816 ± 0.0003	11.1818 ± 0.0004	−0.2	−1.1
SiO-16	1998.410	−26.4235 ± 0.0020	−34.4517 ± 0.0027	2.6	−0.3
	2000.850	−26.4217 ± 0.0006	−34.4413 ± 0.0011	−3.2	−1.2

Table A1
(Continued)

Name	Epoch	R.A. Offset[a] (arcsec)	Decl. Offset (arcsec)	ΔR.A.[a] (mas)	ΔDecl. (mas)
	2006.200	−26.4190 ± 0.0006	−34.4553 ± 0.0013	2.5	3.5
	2008.860	−26.4183 ± 0.0010	−34.4473 ± 0.0025	−3.1	−0.9
	2011.470	−26.4181 ± 0.0008	−34.4556 ± 0.0007	1.7	−1.6
	2014.249	−26.4216 ± 0.0005	−34.4696 ± 0.0010	3.0	3.0
	2022.227	−26.4205 ± 0.0002	−34.4832 ± 0.0004	2.8	3.2
SiO-6	1998.410	35.2203 ± 0.0029	30.6532 ± 0.0050	−2.7	0.9
	2000.850	35.2324 ± 0.0006	30.6595 ± 0.0010	3.6	0.5
	2006.200	35.2449 ± 0.0010	30.6702 ± 0.0028	−3.4	−3.2
	2008.860	35.2486 ± 0.0009	30.6793 ± 0.0049	3.5	0.3
	2011.470	35.2658 ± 0.0020	30.6878 ± 0.0040	−1.5	2.1
	2014.249	35.2725 ± 0.0018	30.7022 ± 0.0019	−3.8	−2.5
	2020.988	35.2838 ± 0.0005	30.7059 ± 0.0016	1.1	−2.5
	2022.227	35.2945 ± 0.0008	30.7144 ± 0.0019	−3.7	−2.8
SiO-17	1998.410	8.0426 ± 0.0005	−27.7032 ± 0.0014	1.2	1.3
	2006.200	8.0623 ± 0.0005	−27.6852 ± 0.0009	−0.9	2.7
	2008.860	8.0698 ± 0.0008	−27.6760 ± 0.0004	−0.7	−2.0
	2011.470	8.0719 ± 0.0006	−27.6652 ± 0.0010	1.5	0.3
	2014.249	8.0818 ± 0.0002	−27.6648 ± 0.0004	−0.4	2.8
	2020.988	8.0988 ± 0.0005	−27.6453 ± 0.0011	−1.6	−0.0
	2022.227	8.1013 ± 0.0002	−27.6431 ± 0.0005	−0.6	2.8
SiO-11	1998.410	1.7380 ± 0.0023	40.2675 ± 0.0032	−2.1	−1.1
	2000.850	1.7400 ± 0.0005	40.2795 ± 0.0011	1.8	2.6
	2006.200	1.7462 ± 0.0005	40.2914 ± 0.0006	−0.0	−4.0
	2008.860	1.7475 ± 0.0003	40.2954 ± 0.0008	1.9	2.4
	2011.470	1.7590 ± 0.0002	40.3034 ± 0.0004	−2.2	0.3
	2014.249	1.7610 ± 0.0003	40.3119 ± 0.0010	−0.7	−3.8
	2020.988	1.7708 ± 0.0003	40.3168 ± 0.0005	2.2	−0.7
	2022.227	1.7759 ± 0.0003	40.3240 ± 0.0005	−0.4	−4.0
IRS 17	2000.850	13.1502 ± 0.0026	5.5651 ± 0.0025	1.1	−0.2
	2006.200	13.1414 ± 0.0013	5.5611 ± 0.0021	−1.3	−0.6
	2008.860	13.1445 ± 0.0010	5.5554 ± 0.0056	1.0	−0.2
	2014.249	13.1359 ± 0.0023	5.5513 ± 0.0017	−1.3	−0.4
	2020.988	13.1270 ± 0.0036	5.5443 ± 0.0081	0.1	−0.8
	2022.227	13.1262 ± 0.0022	5.5437 ± 0.0048	−1.3	−0.5
SiO-12	2000.850	−18.8236 ± 0.0028	42.4687 ± 0.0032	0.5	3.6
	2006.200	−18.8211 ± 0.0017	42.4459 ± 0.0050	2.0	−4.1
	2008.860	−18.8164 ± 0.0018	42.4647 ± 0.0025	0.7	3.4
	2011.470	−18.8091 ± 0.0010	42.4721 ± 0.0020	−2.4	−0.8
	2014.249	−18.8113 ± 0.0005	42.4820 ± 0.0011	1.2	−4.3
	2020.988	−18.8030 ± 0.0007	42.4850 ± 0.0027	2.6	0.4
	2022.227	−18.8009 ± 0.0008	42.4910 ± 0.0012	1.6	−4.3
IRS 19NW	1998.410	14.5516 ± 0.0011	−18.4617 ± 0.0012	0.5	1.3
	2000.850	14.5533 ± 0.0015	−18.4683 ± 0.0031	0.2	−1.8
	2006.200	14.5606 ± 0.0005	−18.4656 ± 0.0009	−1.5	1.8
	2008.860	14.5620 ± 0.0010	−18.4695 ± 0.0013	0.1	−1.8
	2011.470	14.5625 ± 0.0004	−18.4638 ± 0.0008	1.1	0.7
	2014.249	14.5706 ± 0.0003	−18.4729 ± 0.0007	−1.1	2.0
	2020.988	14.5793 ± 0.0003	−18.4753 ± 0.0008	−1.2	−0.5
	2022.227	14.5815 ± 0.0001	−18.4768 ± 0.0002	−1.3	1.9

Notes. Coordinate offsets are with respect to the Sgr A* radio centroid at each epoch. The relative differential offsets listed in the last two columns and described in Section 3 have been subtracted from the coordinate offsets.
[a] This offset is corrected for decl.: it is ΔR.A.cos(decl.).
[b] The first two epochs were not used for the IRS 7 astrometry but are included here for posterity.

Appendix B
Proper Motion Measurement Methods

Some of the time series in Figure 3 show large single-epoch outliers from secular trends. To address the impact of these outliers on proper motion measurements, we explored three different proper motion fitting methods: (1) variance-weighted LS; (2) a "conservative formulation" of uncertainties (Sivia & Skilling 2006; Darling et al. 2018); and (3) a "good-and-bad data" model (Box & Tiao 1968; Sivia & Skilling 2006). Details on all three methods are presented here.

1. The weighted LS method minimizes the variance-weighted difference between the model and the data. For proper motions, the data are simply the coordinate time series, and the model is a line (slope and intercept). For this method and the following fitting methods, we assign the reference epoch to be the coordinate variance-weighted mean of all observation epochs. The coordinate variance at each epoch is the sum in quadrature of the uncertainty in each coordinate. For linear fitting, all epochs are relative to the reference epoch, and the intercept of the proper motion fit is the coordinate at the reference epoch. This approach minimizes the correlation between the slope and intercept of linear fits. We used `lmfit` (Newville et al. 2021) for the minimization.

We simultaneously fit the proper motions in both coordinates in order to assess correlations between fit parameters and any cross talk between nominally orthogonal proper motions. There can be a minor correlation between the slope and intercept of single-coordinate fits because one reference epoch is used for both coordinates. Correlation between R.A. and decl. solutions is generally negligible.

2. The "conservative formulation" does not assume Gaussian measurement uncertainties. Instead, it treats error bars as lower bounds and assigns slowly decaying tails to the probability distribution, which can reduce the impact of outlier data points (Sivia & Skilling 2006). In this paradigm, the probability of an error-weighted data-model residual R_i for data point i, given a model, is

$$\mathrm{prob}(R_i) \propto \frac{1 - e^{-R_i^2/2}}{R_i^2}. \tag{B1}$$

We maximize the sum of the logarithm of this probability (the posterior probability density) to estimate the model parameters and their marginalized uncertainties using `emcee` (Foreman-Mackey et al. 2013). The four model parameters are generally uncorrelated.

3. The "good-and-bad data" model assumes that the uncertainties in measurements are underestimated by a factor γ with probability β such that (Box & Tiao 1968; Sivia & Skilling 2006)

$$\mathrm{prob}(R_i) \propto \left(\frac{\beta}{\gamma} e^{-R_i^2/2\gamma} + (1 - \beta) e^{-R_i^2/2}\right). \tag{B2}$$

This effectively introduces two additional parameters to the proper motion fits, for a total of six (a slope and intercept for each coordinate, γ, and β). It is worth noting that this method does not identify individual "bad" data points.

As with the conservative formulation, we maximize the sum of the logarithm of the probability using a Markov Chain Monte Carlo (MCMC) process. We place bounds (uniform priors) on the two good-and-bad parameters: $0 \leqslant \beta \leqslant 1$ and $1 \leqslant \gamma \leqslant 10$. β and γ tend to be anticorrelated (a lower probability of bad data drives larger uncertainties) and are often correlated with the linear fit parameters. Values for β are typically 0.3–0.8 and for γ are 2–4, which represent a high probability that the data have variances a factor of several too small. Nevertheless, this method does not typically produce

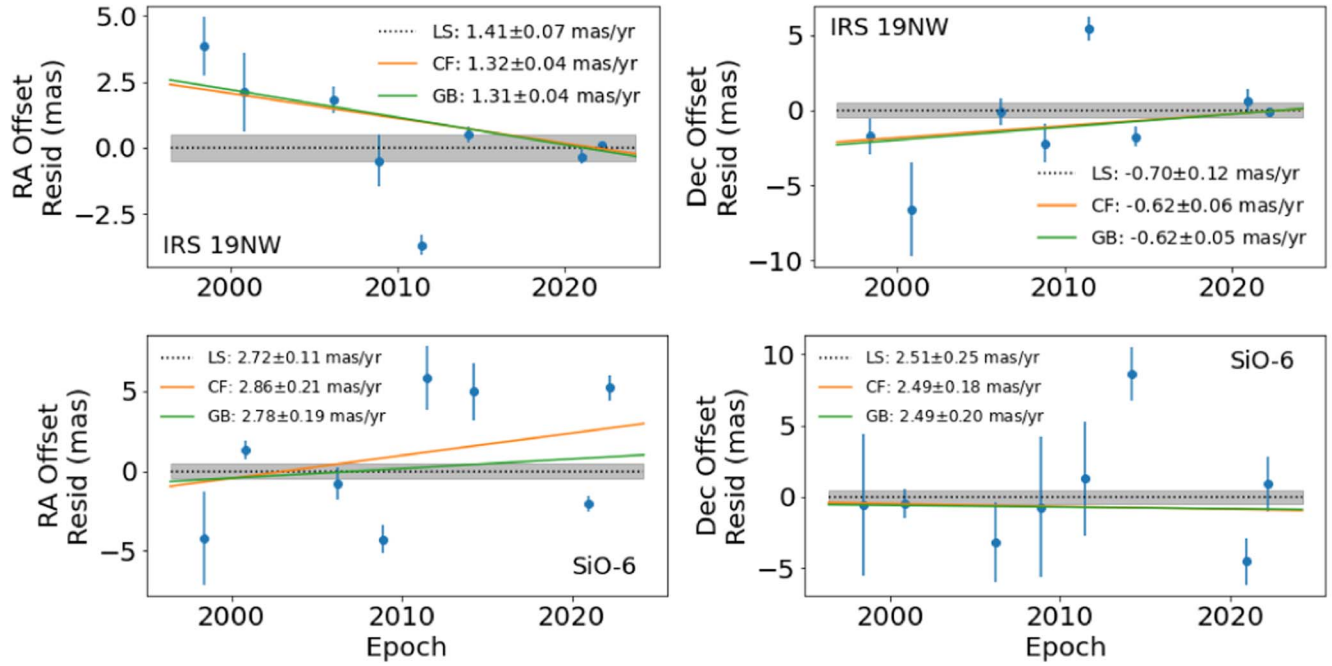

Figure B1. Example residual proper motion time series showing the three fitting methods (LS = least-squares; CF = conservative formulation; GB = good-and-bad data). The residual is with respect to the weighted LS fit, and the shaded regions indicate ±4 au. Top: IRS 19NW, showing proper motion solutions for the conservative formulation and good-and-bad methods that differ from the canonical LS fit. Bottom: SiO-6 shows differing proper motion solutions in R.A. for all three methods. For most of the masers, the two less conventional fitting methods do not improve upon or differ significantly from the LS method. R.A. offsets are true angular offsets (i.e., they are corrected for cos(decl.)).

significantly different proper motion measurements than the simple weighted LS method. There are two masers with large outliers where this method does favor large uncertainty scaling $\gamma \sim 7$–8 and proper motion solutions that differ significantly from the other two methods, namely SiO-11 and IRS 19NW. SiO-6 has $\gamma \sim 5$ and shows a bimodal likelihood distribution in R.A. slope and offset in both alternative methods, but all three slopes are consistent within their error budgets. Figure B1 shows the proper motion fit residuals for IRS 19NW and SiO-6. Note that we did not assign separate β and γ parameters to each coordinate time series.

The majority of maser proper motions obtained from these three fitting methods are indistinguishable given their uncertainties, so we report the LS fits in Table 2 and Figure 3. Because the conservative formulation and good-and-bad data methods allow for larger uncertainties in the data, they would normally be expected to produce larger uncertainties in parameter estimates than variance-weighted LS fits. However, contrary to what is expected for uniform Gaussian random errors, the proper motion uncertainties are typically, but not exclusively, larger for the LS method compared to the other two methods. When $\chi^2_\nu \sim 1$ (see Table 2), uncertainties in the alternative methods are larger than for the LS estimates, following the canonical expectation.

Appendix C
Expanded Astrometric Uncertainties

To assess the large astrometric departures from secular trends seen in Figure 3, we quantify a time-independent additional uncertainty that could be added in quadrature to the measurement uncertainties quoted in Table A1. To do this, we adopt a linear-fit model that includes an additional uncertainty parameter for each coordinate. Starting with the variance-weighted LS solutions, we perform an initial (log) likelihood maximization fit followed by an MCMC exploration of the parameter space using `emcee` (Foreman-Mackey et al. 2013) to estimate uncertainties in the new fit parameters. This process effectively finds the additional constant uncertainty that would be included in the time series in order to maximize the likelihood of a linear fit.

For three (20%) of the masers, the EUs are negligible (less than 0.1 mas) compared to the measurement uncertainties in both coordinates. For six (40%) of the masers, one of the two coordinates favors a significant increase in astrometric uncertainty. These range from 0.3 to 2.1 mas and favor the R.A. direction over decl. (4 versus 2). For the remaining six (40%), both coordinate time series have significant uncertainty increases, spanning 1.7–8.5 mas, and are always larger for decl. compared to R.A. In the latter two groups, however, the proper motions obtained from the MCMC process that allows for expanded uniform (time-independent) uncertainties are formally consistent with the LS proper motions that rely on the original measurement uncertainties. This treatment does not obtain different proper motions from the basic LS method.

Figure C1 shows example fits for the same masers depicted in Figure B1, IRS 19NW and SiO-6. The proper motions are not formally different from the LS values, but it is clear that the expanded astrometric uncertainties are much larger than the expected size of the maser-emitting region in these stars, suggesting that the departures from the linear trends are not simply due to the changing structure of the maser-emitting regions.

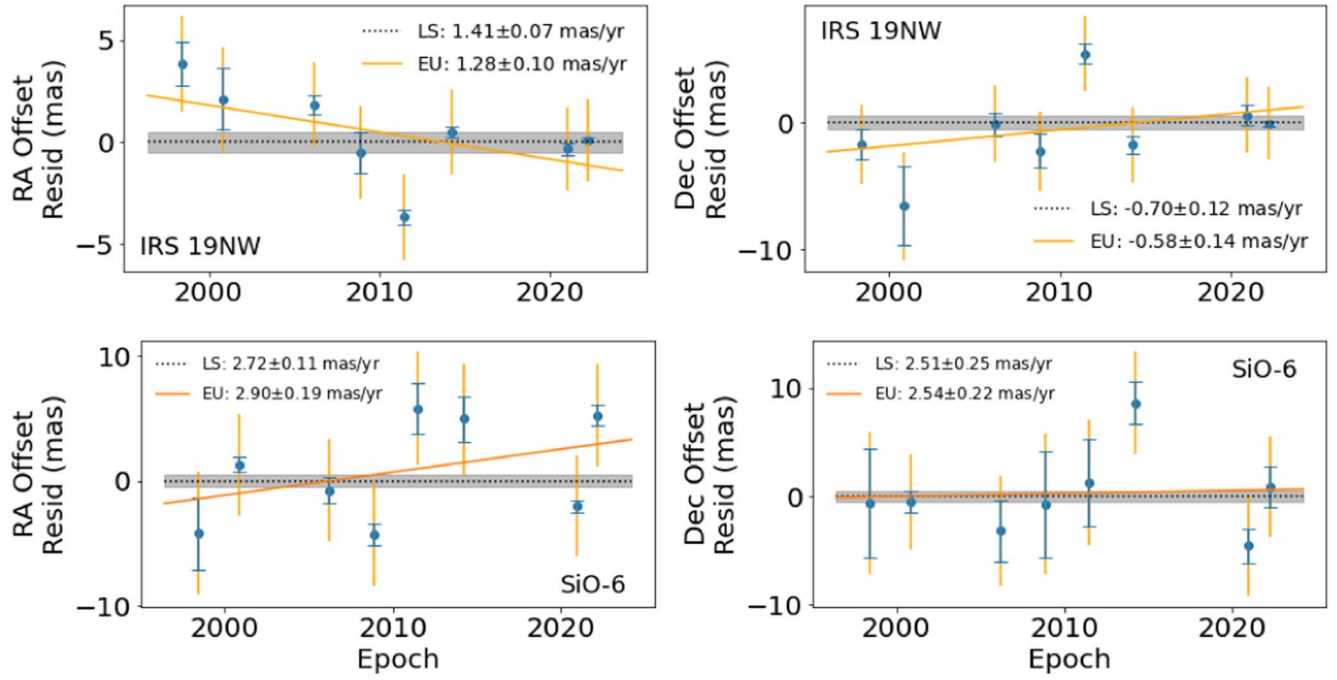

Figure C1. Example residual proper motion time series showing the result of EUs that are added in quadrature to the measurement uncertainties (see Appendix C). The residual is with respect to the weighted LS fit, and the shaded regions indicate ±4 au. Top: IRS 19NW shows proper motion solutions that differ from the canonical LS fits but are formally consistent given the uncertainties. The additional uncertainties are 2.0 mas in R.A. and 2.8 mas in decl. Bottom: SiO-6 shows a differing proper motion solution in R.A. but not in decl., which have EUs of 4.0 and 4.3 mas, respectively. R.A. offsets are true angular offsets (i.e., they are corrected for cos(decl.)).

ORCID iDs

Jeremy Darling https://orcid.org/0000-0003-2511-2060
Jennie Paine https://orcid.org/0000-0002-7517-9223
Mark J. Reid https://orcid.org/0000-0001-7223-754X
Karl M. Menten https://orcid.org/0000-0001-6459-0669
Shoko Sakai https://orcid.org/0000-0001-5972-663X
Andrea Ghez https://orcid.org/0000-0003-3230-5055

References

Astropy Collaboration, Robitaille, T. P., Tollerud, E. J., et al. 2013, A&A, 558, A33
Box, G. E. P., & Tiao, G. C. 1968, J. Am. Stat. Assoc., 63, 174
Comrie, A., Wang, K.-S., Hsu, S.-C., et al. 2021, CARTA: The Cube Analysis and Rendering Tool for Astronomy, Astrophysics Source Code Library, ascl:2103.031, v2.0.0, Zenodo, doi:10.5281/zenodo.4905459
Cotton, W. D., Perrin, G., & Lopez, B. 2008, A&A, 477, 853
Darling, J. 2022, ApJL, 931, L14
Darling, J., Truebenbach, A. E., & Paine, J. 2018, ApJ, 861, 113
Do, T., Hees, A., Ghez, A., et al. 2019, Sci, 365, 664
Ellis, G. F. R., & Baldwin, J. E. 1984, MNRAS, 206, 377
Foreman-Mackey, D., Hogg, D. W., Lang, D., & Goodman, J. 2013, PASP, 125, 306
Genzel, R., Eisenhauer, F., & Gillessen, S. 2010, RvMP, 82, 3121
Ghez, A. M., Salim, S., Weinberg, N. N., et al. 2008, ApJ, 689, 1044
GRAVITY Collaboration, Abuter, R., Aimar, N., et al. 2022, A&A, 657, L12
GRAVITY Collaboration, Abuter, R., Amorim, A., et al. 2020, A&A, 636, L5
Gravity Collaboration, Abuter, R., Amorim, A., et al. 2021, A&A, 647, A59
Heißel, G., Paumard, T., Perrin, G., & Vincent, F. 2022, A&A, 660, A13
Hunter, J. D. 2007, CSE, 9, 90
Kaplan, G. H. 2005, USNOC, 179
Lacroix, T. 2018, A&A, 619, 46
Leung, H. W., Bovy, J., Mackereth, J. T., et al. 2023, MNRAS, 519, 948
Li, J., An, T., Shen, Z.-Q., & Miyazaki, A. 2010, ApJL, 720, L56
McMullin, J. P., Waters, B., Schiebel, D., Young, W., & Golap, K. 2007, in ASP Conf. Ser., Astronomical Data Analysis Software and Systems XVI, ed. R. A. Shaw, F. Hill, & D. J. Bell (San Francisco, CA: ASP), 127
Menten, K. M., Reid, M. J., Eckart, A., & Genzel, R. 1997, ApJL, 475, L111
Nampalliwar, S., Kumar, S., Jusufi, K., et al. 2021, ApJ, 916, 116
Newville, M., Otten, R., Nelson, A., et al. 2021, lmfit/lmfit-py, v1.0.3, Zenodo, doi: 10.5281/zenodo.5570790
Paine, J., & Darling, J. 2022, ApJ, 927, 181
Plewa, P. M., Gillessen, S., Eisenhauer, F., et al. 2015, MNRAS, 453, 3234
Price-Whelan, A. M., Sipőcz, B. M., Günther, H. M., et al. 2018, AJ, 156, 123
Reid, M. J., & Brunthaler, A. 2020, ApJ, 892, 39
Reid, M. J., Menten, K. M., Brunthaler, A., et al. 2019, ApJ, 885, 131
Reid, M. J., Menten, K. M., Genzel, R., et al. 2003, ApJ, 587, 208
Reid, M. J., Menten, K. M., Trippe, S., Ott, T., & Genzel, R. 2007, ApJ, 659, 378
Sakai, S., Lu, J. R., Ghez, A., et al. 2019, ApJ, 873, 65
Schödel, R., Gallego-Cano, E., Dong, H., et al. 2018, A&A, 609, A27
Sivia, D. S., & Skilling, J. 2006, Data Analysis—A Bayesian Tutorial (2nd ed.; Oxford: Oxford Univ. Press)
Smoot, G. F., Gorenstein, M. V., & Muller, R. A. 1977, PhRvL, 39, 898
van der Walt, S., Colbert, S. C., & Varoquaux, G. 2011, CSE, 13, 22
Weinberg, N. N., Milosavljević, M., & Ghez, A. M. 2005, in ASP Conf. Ser., 338, Astrometry in the Age of the Next Generation of Large Telescopes, ed. P. K. Seidelmann & A. K. B. Monet (San Francisco, CA: ASP), 252
Xu, S., Zhang, B., Reid, M. J., et al. 2022, ApJ, 940, 15
Yelda, S., Lu, J. R., Ghez, A. M., et al. 2010, ApJ, 725, 331
Yuan, G.-W., Shen, Z.-Q., Tsai, Y.-L. S., Yuan, Q., & Fan, Y.-Z. 2022, PhRvD, 106, 103024